JOURNAL OF PROPULSION AND POWER
Vol. 21, No. 1, January–February 2005

Prediction of High-Pressure Turbine Main-/Secondary-Air System Flow Interaction

Roger L. Davis*
University of California, Davis, Davis, California 95616
Juan J. Alonso†
Stanford University, Stanford, California 94305
Jixian Yao‡
General Electric Global Research Center, Niskayuna, New York 12309
and
Roger Paolillo§ and Om P. Sharma¶
Pratt and Whitney, East Hartford, Connecticut 06108

The results from a steady, viscous flow simulation of the main flowpath of a modern jet engine transonic high-pressure turbine, transition duct, and first vane of the low-pressure turbine, coupled with the secondary-air system under the high-pressure turbine, is presented. The secondary-air system configuration includes the lower cavity near the centerline, the mid-cavity with the tangential onboard injection nozzle and pump, and the upper rim cavity. In addition, the flow through the inner tangential onboard injection seal and labyrinth seals that separate the cavities is included. The purpose of this investigation is to determine the feasibility of the use of computational procedures to predict the steady-flow interaction effects between the main- and secondary-air system flow, the ability to predict flow splits in the secondary-air system, and the numerical issues associated with such a computation. A description of the numerical procedure, along with technical details of the initial and boundary conditions and convergence of the numerical procedure are presented. Details of the predicted flow physics in the secondary-air system flowpath, including the rim-cavity and inner tangential onboard injection/labyrinth seals, the main flowpath, and the interaction region at the junction between the two flowpaths are presented. The effect of the secondary-air system flow on the aerodynamic performance and hub endwall temperature distribution of the main flowpath blade rows is also discussed.

Nomenclature

A	=	cross section area
c_p	=	coefficient of specific heat at constant pressure
M	=	Mach number
$\dot{m}$	=	mass flow rate
P	=	pressure
R	=	gas constant for air
T	=	temperature
γ	=	ratio of specific heats
ρ	=	density

Subscripts

exit	=	secondary-air exit conditions
in	=	secondary-air inlet conditions
pres	=	prescribed condition
t_{exit}	=	stagnation conditions at exit
t_{in}	=	stagnation conditions at inlet

Received 19 July 2003; presented as Paper 2003-4833 at the AIAA/ASME/SAE/ASEE 39th Joint Propulsion Conference, Huntsville, Alabama, 20 July 2003; revision received 18 January 2004; accepted for publication 5 February 2004.

*Professor, Stanford Consulting Professor, Mechanical and Aeronautical Engineering Department. Senior Member AIAA.
†Assistant Professor, Aeronautical and Astronautical Engineering Department. Member AIAA.
‡Research Engineer, Computational Fluid Dynamics Department.
§Discipline Chief, Air Systems Design-Integration Department.
¶Chief Technologist.

Introduction

THE design of modern gas-turbine engines has increasingly relied on the use of three-dimensional computational fluid dynamics procedures to optimize aerodynamic performance, reduce weight and cost, and maximize durability. Several numerical procedures have been developed to predict the flows in the compressor and turbine turbomachinery components of the gas-turbine engine. These procedures can solve for either the steady or unsteady flow through multistages of those components.

Steady-flow predictions are often used as a three-dimensional detailed extension of through-flow analysis and are especially useful as a design tool. The steady-flow prediction methodology only requires the solution of a single passage of each blade row in the machine. A mixing-plane boundary condition, in which the primary variables or fluxes are circumferentially averaged and exchanged at the interfaces between blade rows is used to communicate the axisymmetric flow through the machine. As such, steady-flow predictions can be performed with relatively fast turnaround solution times and reasonable computer resources. These solutions provide information regarding work-load distributions, aerodynamic performance (efficiency), and airfoil pressure loading. In addition, these steady-state solution procedures can also be used to predict the radial distribution of heat loads (in the absence of circumferentially varying hot streaks) through the machine, which is especially important for the turbine.

Combustor burners often produce temperature peaked profiles that can enter the turbine where they interact with the turbine blade and accumulate in the time-averaged flow toward the blade pressure side and near the tip. The temperature profile at the exit of the combustor may be biased by design toward the hub endwall of the turbine to avoid blade tip and outer air-seal burning due to hot-streak migration. In this case, however, the hot gases from the combustor can be ingested into the rim cavity that separates the high-pressure turbine vane and blade. If large amounts of gases are ingested, the

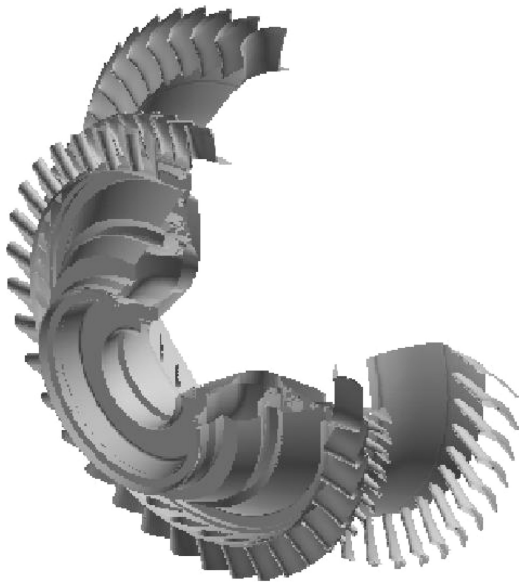

Fig. 1 HPT stage with secondary-air system, TD, first vane LPT configuration.

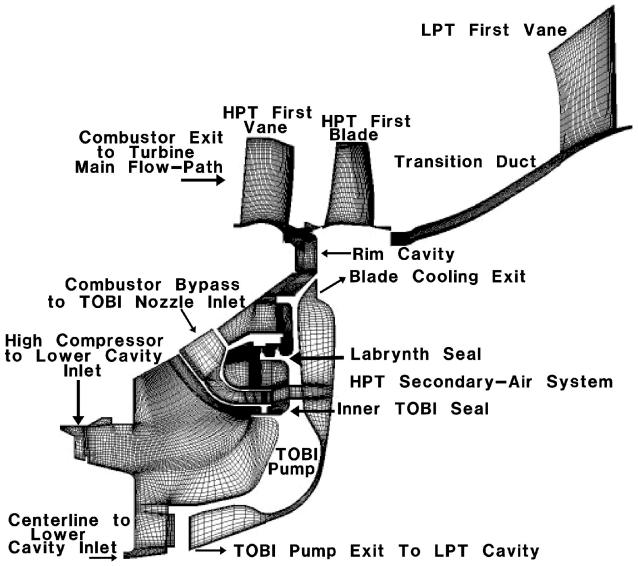

Fig. 2 Main flowpath and secondary-air system computational grid (every other grid point shown).

temperature near the hub and in the rim cavity can become supercritical, leading to burning of the hub platform and blade disk.

To avoid hot-gas ingestion into the rim cavity, compressor bypass air is used to purge the disk and rim cavities and maintain a positive leakage flow back into the turbine main flowpath. During the design, a one-dimensional flow network analysis is typically used to predict the pressure and flow rate necessary to maintain this positive leakage flow and prevent hot-gas ingestion into the rim cavity. In predictions of the turbine main flowpath, leakage flows through gaps in the hub and casing endwalls between the rotating and stationary blade rows are typically modeled with a prescribed transpiration or injection boundary condition treatment in the computational fluid dynamic procedure. The mass flow and stagnation temperature of the leakage flow are typically based on the one-dimensional network analysis.

Because of the limitations in the one-dimensional network analysis and the complex flow physics at the hub where the rim-cavity flow interacts with the main flowpath, designs can often have either too little purge flow, resulting in hot-gas ingestion and disk and/or hub burning, or too much purge flow, resulting in lost engine thrust and degraded engine efficiency. Any inaccuracy in the network analysis prediction in purge flow also effects the main flowpath predictions. Thus, there has been a desire to use more sophisticated analyses, including computational fluid dynamics, to predict the flow in the secondary air-system and its interaction with the main flowpath. It is believed that with additional fidelity in the analysis, the reliability and accuracy of the predictions can increase, thereby leading to further optimization in the amount of purge flow and the secondary-air system geometry.

This paper presents the predicted results in which the secondary-air system is coupled directly with the main flowpath of a modern high-pressure turbine (HPT) in a single computational fluid dynamic simulation. Several issues, including placement of the main flowpath interblade row mixing plane treatment, boundary conditions, flow initialization, and computational efficiency are discussed. The flow physics in the various regions of the secondary-air system, including the lower centerline cavity, the tangential onboard injection (TOBI) pump, the midcavity, the inner TOBI and labyrinth seals, and the rimcavity are presented. The effect of the secondary-air system flow on the performance of the main flowpath blade rows is also discussed, and results are compared with those from isolated main flowpath simulations in which the hub leakage flow is modeled with a transpiration boundary condition.

Configuration

Figure 1 shows the transonic HPT stage, transition duct (TD), and low-pressure turbine (LPT) first vane in the main flowpath along with the HPT secondary-air system that was used in the present numerical investigation. This geometry is representative of a modern HPT design consisting of 36 and 60 HPT vanes and blades, respectively, and 48 LPT first vanes. The secondary-air system is modeled as an effective axisymmetric representation of the real geometry, but with three-dimensional flow to reduce the computational grid requirements. The circumferential extent of the secondary-air system is the same as the HPT blade.

As shown in Fig. 2, flow enters the secondary-air system near the centerline and mid-way radially in the lower secondary-air system cavity. This air comes from the high-pressure compressor (HPC). In addition, air enters the TOBI nozzle from the combustor burner bypass. Flow exits the high-pressure secondary-air system near the centerline, where it passes to the LPT secondary-air system. In addition, flow exits between the TOBI pump and the blade disk near the top of the TOBI pump, where it proceeds into the HPT blade as film-cooling air (not modeled in the current simulation). Finally, some of the air from the secondary-air system exits into the main flowpath at the top of the rim cavity. This air is critical to maintain a positive purge from the secondary-air system into the main flowpath to keep combustor hot gases from being ingested into the rim cavity and burning the blade disk. The boundary conditions used for the inlets and exits of the secondary-air system were determined from a one-dimensional network analysis used during the preliminary design of the secondary-air system.

Swirl vanes that are present at the end of the TOBI nozzle are absent from the present simulation. A body-force model has been implemented in the current numerical procedure to swirl the flow in place of the TOBI vanes. Also, holes in the TOBI pump at the end of the TOBI nozzle have been replaced with a slot with the same effective area as the holes. These modifications were made in the numerical model to simplify grid generation and reduce the computational grid requirements.

Numerical Simulation

The three-dimensional, multiblock, parallel flow solver, TFLO[1] has been developed under the U.S. Department of Energy (DoE) Advanced Strategic Computing Initiative (ASCI) program in an effort to step up to large-scale parallel steady- and unsteady-flow multistage turbomachinery simulations. The Reynolds-averaged Navier–Stokes equations are solved in the TFLO procedure via a cell-centered discretization on arbitrary multiblock meshes. The solution algorithm is based on an efficient explicit five-stage Runge–Kutta integration scheme[2] coupled with multigrid, implicit residual smoothing, and local time-stepping convergence acceleration techniques. Wilcox's[3] k–ω two-equation turbulence model is used to predict the

turbulence viscosity in the field. The solver is parallelized by the use of domain decomposition, a single program multiple data strategy, and the message passing interface (MPI) standard. Validation of the TFLO procedure for steady and unsteady turbine flows is presented in Refs. 1, 4, and 5.

Computational Grid

Figure 2 shows the multiblock structured grid used in the main-/secondary-air system flowpaths. (Note that every other grid point is shown.) The secondary-air system computational grid is point matched to a grid block constructed to extend across the main flowpath between the end of the HPT stator hub and the beginning of the rotating HPT blade hub. Communication between the main- and secondary-air system flows in TFLO do not have to be performed directly with point-matched grids, however. A special interface that allows point-mis-matched grids to be used across any block boundary[6] may be used as an alternative to point-matched grids to eliminate grid stretching or skew problems that might occur. This special interface allows different computational grid systems or non point-matched grids to communicate with each other through use of a three-dimensional interpolation process. In addition, this interface allows for multiple TFLO executions (each possibly corresponding to a different flow region) to run and communicate with each other in parallel.

An H-grid was used to discretize the main flowpath. The mesh sizes used for the main flowpath, in the axial times circumferential times radial directions, can be summarized as follows: first vane, $129 \times 57 \times 81$; strip block to merge with secondary-air system, $33 \times 57 \times 81$; rotor, $129 \times 57 \times 81$ for the main passage: and $97 \times 33 \times 17$ for the tip gap, transition duct, and second vane, $377 \times 57 \times 81$. This resulted in a total of approximately three million grid points for the main flowpath, which, based on previous numerical experiments, was considered to provide essentially grid independence. A total of 97 points where used in the axial direction along the airfoil chord between the leading and trailing edges for each airfoil row. The secondary-air system grid consisted of 183 structured grid blocks with approximately six million grid points resulting in a total of approximately nine million points for the coupled simulation. The grid density used in the secondary-air system was held at levels proportional to that used in the main flowpath based on the volume and solid surface area ratios. The wall spacing was approximately 2.0×10^{-5} everywhere in the domain, except in some local areas of the secondary-air system where compromises in wall spacing were necessary to keep the grid density affordable. The steady-flow simulation was executed on nine nodes (144 processors) of the DoE Frost Pacific IBM SP3 at Lawrence Livermore Laboratory. The total turnaround time for this initial baseline simulation was approximately 105 days.

Boundary and Initial Conditions

The flow conditions used for this investigation correspond to the design cruise conditions. At the inlet to the main flowpath, a uniform total pressure with a 3%-span boundary-layer thickness, a purely axial flow angle, and a top-hat radial total temperature profile representative of the combustor exit flow were used as the boundary condition. A uniform exit static pressure was held as the exit boundary condition downstream of the LPT vane in the main flowpath. When the exit static to inlet total pressure ratio in the main flowpath is held, the mainstream flow rate was predicted as part of the overall solution. All solid walls in both the main- and secondary-air system flowpaths were assumed to be adiabatic. The film cooling flow on the HPT vane and blade has been neglected in the current simulation. The freestream turbulence intensity was assumed to be 1.0% at all inlets.

At the three different inlets to the secondary-air system, the stagnation temperature and absolute flow angle were held fixed to specified values determined from a one-dimensional network design analysis. In addition, either the stagnation pressure or mass flow rate may be prescribed. If stagnation pressure is held, then the total mass flow rate and its distribution through the secondary-air system is predicted. It was found that this boundary condition treatment could result in negative flow at the secondary-air system inlets and exits due to the large transients in pressure during convergence. In the current investigation, the mass flow through each of the secondary-air system inlets was prescribed to be the same as that determined from the one-dimensional network analysis. As a result, the total flow going into the secondary-air system could be controlled and set to be the same as the design intent. The flow angle was held to be normal to each inlet boundary. The mass flux computed from the specified mass flow $\dot{m}_{\text{in}}$ and inlet area A_{in} is used to determine the inlet density from the enthalpy relationship and equation of state according to

$$\rho_{\text{new}} = \left[\frac{P}{R} + \sqrt{\left(\frac{P}{R}\right)^2 + \frac{2T_{t_{\text{in}}}(\dot{m}_{\text{in}}/A_{\text{in}})^2}{c_p}} \right] \Bigg/ 2T_{t_{\text{in}}} \qquad (1)$$

where P is the static pressure extrapolated in the direction normal to the boundary from inside of the domain and $T_{t_{\text{in}}}$ is the specified stagnation temperature. Once the inlet density is determined, the velocity components are computed from the prescribed mass flow rate and inlet area under the assumption that the flow angle is normal to the inlet. It can be shown that this boundary condition treatment is the same as the extrapolation of the static temperature and an iterative change of the inlet total pressure until the desired flow rate is obtained.

One of two possible boundary condition treatments may be used at the exits of the secondary-air system. At these exits, the static pressure or the mass flow rate may be held at a specified value. The flow rate through each of the secondary-air system exits and, thus, the flow splits, are predicted if the exit static pressure is prescribed. If the mass flow rate through each exit is prescribed, then the exit pressure of each secondary-air system exit is automatically adjusted, first by calculation of the exit Mach number M_{exit} from the total mass flow parameter through the iterative solution of

$$M_{\text{exit}} \left[1 + \frac{(\gamma - 1)}{2} M_{\text{exit}}^2 \right]^{-(\gamma+1)/[2(\gamma-1)]} = \frac{\dot{m}_{\text{pres}} \sqrt{(T_{t_{\text{exit}}} R)/\gamma}}{P_{t_{\text{exit}}} A_{\text{exit}}} \qquad (2)$$

where $\dot{m}_{\text{pres}}$ is the prescribed mass flow rate, $P_{t_{\text{exit}}}$ is the predicted stagnation pressure, $T_{t_{\text{exit}}}$ is the predicted stagnation temperature, and A_{exit} is the area of the exit. Two to three iterations are typically required to determine the exit Mach number from this relationship. Once the exit Mach number is determined, the exit static pressure required to deliver the prescribed mass flow rate can be found from the isentropic total-to-static pressure relationship and the local stagnation pressure.

The primary focus of the current investigation has been on the determination of the ability of computational fluid dynamics to predict the flow physics in the cavities and the interaction between the main- and secondary-air system flow using the same secondary-air system flow splits determined from the one-dimensional network analysis. As such, most of the results shown hereafter correspond to the case where the mass flow rate of each of the secondary-air system exits was prescribed to the one-dimensional network design intent values. However, the predicted flow splits resulting from a similar coupled simulation, in which the static pressure was held at the secondary-air system exits, are also given to further illustrate issues related to coupled simulations.

The mixing plane between the HPT vane and blade required for steady flow simulations was located at the end of the vane hub in the current simulation. By the placement of the mixing plane at this location, the secondary-air system flow was allowed to interact with the blade mainstream flow directly. Of particular interest in the current investigation was the effect of the secondary-air system flow on the blade hub temperature distribution. Therefore, to minimize the effect of the mixing plane on the interaction between the secondary-air system and blade flow, the mixing plane was set at the end of the vane hub. Conversely, if the interaction of the secondary-air system with the vane flow is of more interest, then an alternative to this placement might be to locate the mixing plane at the blade hub leading edge. If mixing planes are used at both the end of the vane hub

and at the blade hub leading edge, then the possibility arises of the use of an axisymmetric analysis for the secondary-air system, rather than allowing for three-dimensional flow. This strategy may have superior convergence and reduced solution time, but it was felt that the solution accuracy may not be sufficient. Further simulations are necessary to determine the effects of interblade-row mixing plane placement on the predicted flow physics in the main-/secondary-air exit region. As mentioned, the secondary-air system had the same circumferential pitch as the blade.

For the present simulation, the initial conditions were set in the secondary-air system to be axial flow at a pressure and temperature equal to that at the junction between the secondary-air system and the main flowpath between the HPT vane and blade. The initial conditions in the main flowpath were set such that the velocity approximately followed the initial velocity triangles of the airfoils, and the pressure and temperature varied linearly between the inlet and the exit. As will be described later, this initialization strategy could be improved by compensation for the swirl in the secondary-air system flow based on the local radius and the blade rotational speed.

Convergence

There are three factors that limit the convergence rate of the coupled simulation to a steady-state solution, the low-speed flow in the secondary-air system, the choking of the flow through the inner TOBI and labyrinth seals, and the regions of recirculating flow downstream of the seals and in the secondary-air system cavities. In the current investigation, the complex flow in the secondary-air system took 1–2 orders of magnitude longer to converge than the flow in the main flowpath and governed the overall convergence of the coupled domain.

The local convergence of the flowfield in the lower portion of the secondary-air system is limited by the low velocity of the fluid. Because the TFLO procedure uses an explicit time integration scheme, the local time-step size is inversely proportional to the local speed of sound. The velocity of the flow in the secondary-air system decreases with radius. Near the centerline, in the lower secondary-air system cavity, the local speed of sound can become very large and, thereby, cause the local time-step size to become very small. Many time steps are required to convect the flow from the lower cavity to the inner TOBI seal just below the TOBI nozzle where the flow rapidly accelerates and chokes.

Global convergence of the flow is also limited by the choked flow in the inner TOBI seal just below the TOBI nozzle and labyrinth seals at the top of the midcavity in the secondary-air system. The incoming flow from either the lower cavity or from the TOBI nozzle inlet must pass through one or both of these seals before making its way to the exit of the rim cavity and into the main flowpath. The flow that makes its way through the holes (modeled as a slot with effective area) of the TOBI pump into the region adjacent to the blade disk can either flow downward to the centerline or upward to the blade hub and into the blade where it becomes blade internal cooling and, ultimately, film-cooling air (not modeled in the current investigation). The lower portion of the flow adjacent to the blade disk flows between the convergent/divergent nozzle created by the lower portion of the TOBI pump. The flow in this region exits near the centerline and migrates into the LPT secondary-air system cavity.

Finally, the recirculating flow behind the seals and in the lower-, mid-, and rim cavity can breakup into multiple recirculating zones during convergence. The natural unsteadiness and flow instability in and around these cavity recirculations also limits the convergence rate.

Predicted Flow Physics

The absolute temperature contours throughout the main- and secondary-air system flow-paths of the converged solution are shown in Fig. 3. The approximate wall locations where solution convergence was monitored, as shown in Fig. 4, are delineated as stationary wall (SW), disk pump (DP), and blade hub leading edge (BHLE). The temperature is nondimensionalized by the maximum

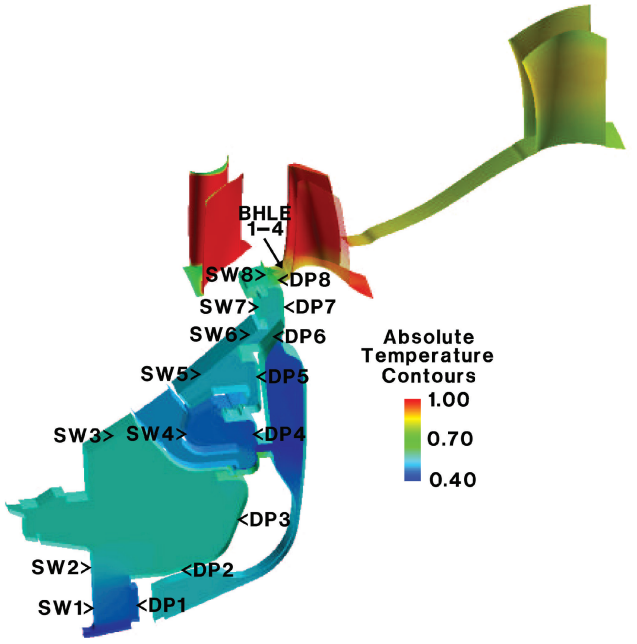

Fig. 3 Main flowpath and secondary-air system absolute temperature contours.

inlet temperature of the main flowpath in Figs. 1–10. The effects of the hot combustor gas is shown to increase the surface temperature in the HPT greatly. However, the cooler temperature from the high compressor permeates the secondary-air system cavities and keeps the temperature much lower. Figure 3 shows that the cooler secondary-air system flow lowers the hub endwall temperature through the blade and into the transition duct.

Figure 4 shows the convergence history of the temperature field in the HPT stage secondary-air system at various points along the SW, the rotating TOBI DP, and the BHLE plane. Figure 4 shows that the temperature field in the secondary-air system takes a significant number of iterations to converge due to the low speed and high swirl in the secondary-air system. The temperature history across the pitch of the HPT blade at the leading edge is also shown in Fig. 4. Four pitchwise stations at 0, 25, 50, and 75% pitch are shown. (Note that 100% pitch is the same as 0% pitch due to periodicity.) Because the flow along the hub at these locations is affected by the secondary-air system flow exiting the rim cavity, it is one of the last regions in the domain to converge. The temperature at midpitch at the blade leading-edge plane decreases significantly during convergence and creates a temperature gradient across the pitch of the blade at the hub. This temperature distribution is described further hereafter.

Figure 5a shows the average nondimensional velocity components in the secondary-air system, and Fig. 5b shows the nondimensionalized total and static pressure and temperature as a function of the radius from the engine centerline. The velocity components were nondimensionalized by the main flowpath inlet total velocity. The pressure was nondimensionalized by the main flowpath inlet total pressure, and, again, the temperature was nondimensionalized by the main flowpath inlet maximum total temperature. Figure 5 shows that the technique used to initialize the flowfield for the current investigation was reasonable. The converged average axial and radial velocity in the secondary-air system is small. The absolute swirl velocity C_u is small at the lower radii and grows in magnitude from the labyrinth seal location outward to the main flowpath. The relative circumferential velocity exiting the secondary-air system into the main flowpath is positive, corresponding to a small negative incidence to the blade at the hub. Improvements in the initialization for the secondary-air system could be made by accounting for the swirl.

Contours of the absolute Mach number along with streamlines constrained to the X, R plane are shown in Fig. 6. The Mach number in the secondary-air system is lowest near the engine centerline

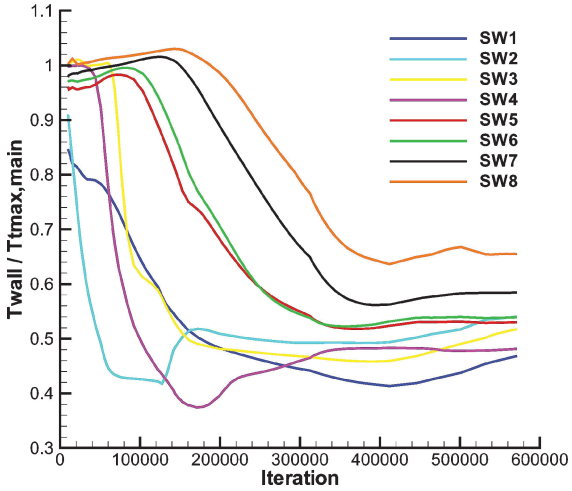

a) SW temperature history

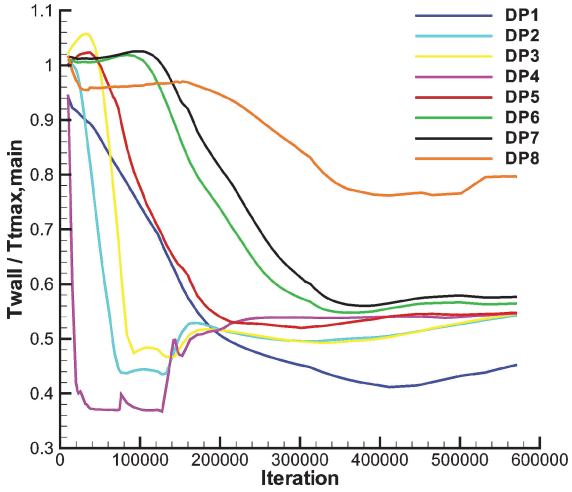

b) DP temperature history

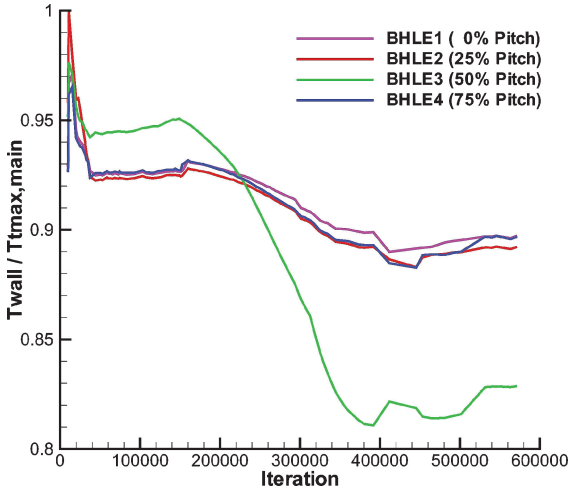

c) BHLE temperature history

Fig. 4 Computed temperature history at various points in HPT secondary-air system and main flowpaths.

and is high at the exit of the TOBI nozzle as the flow enters the TOBI pump slot, as well as in the vicinity of the seals. The streamlines shown in Fig. 6 illustrate the various recirculating regions in the secondary-air system flow. However, the streamlines as shown constrained to the X, R plane are somewhat misleading. By far, the largest component of the velocity in most regions of the secondary-air system, except in the TOBI nozzle and near each inlet, is the circumferential (swirl) velocity. The unconstrained streamlines project

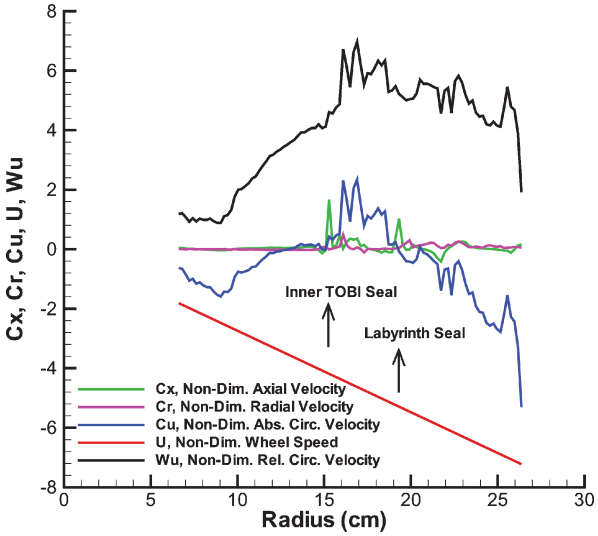

a) Average nondimensional velocity components

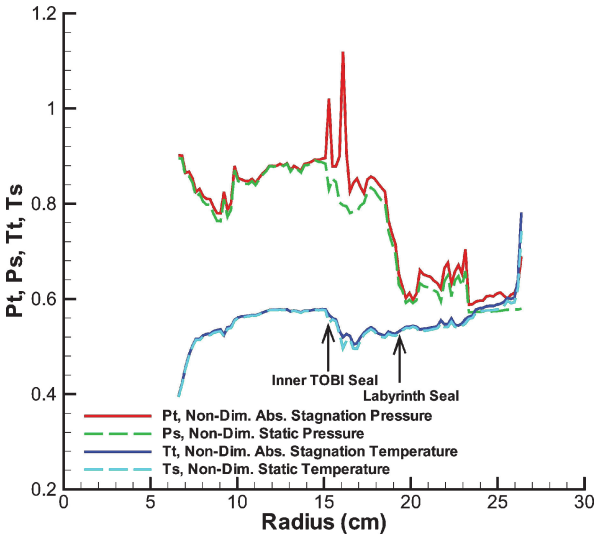

b) Average nondimensional pressure and temperature

Fig. 5 Average nondimensional velocity, pressure, and temperature in secondary-air system flowpath.

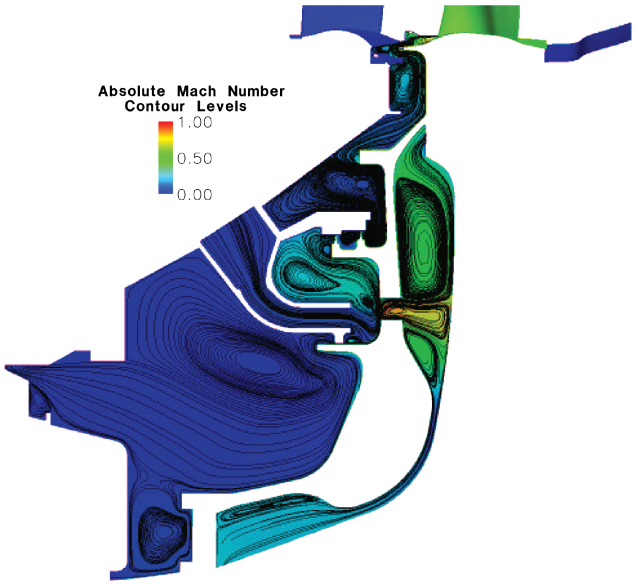

Fig. 6 Secondary-air system absolute Mach number contours and streamlines (limited to axisymmetric plane).

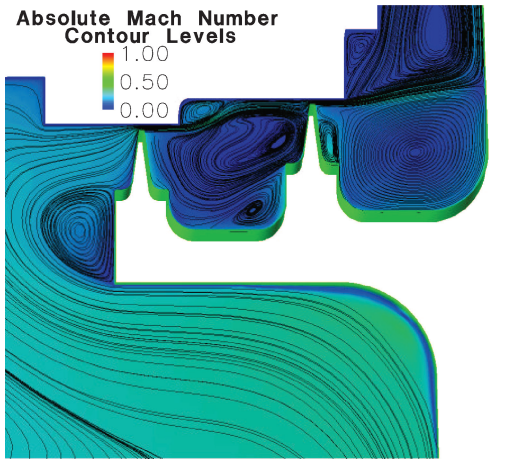

a) Labyrinth seal

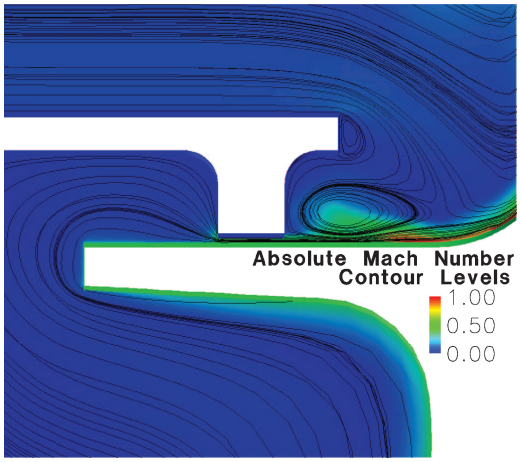

b) Inner TOBI seal

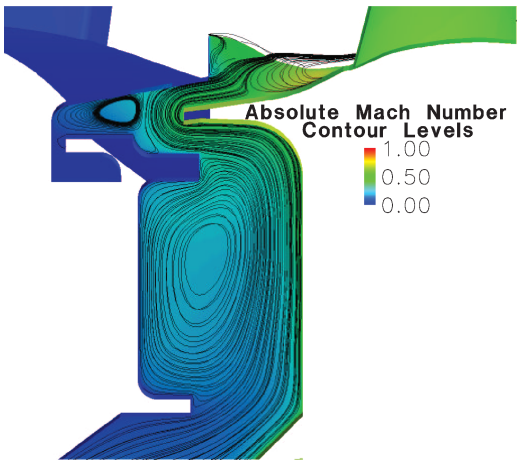

c) Rim cavity

Fig. 7 Close-up of absolute Mach number contours and streamlines (confined to *X*, *R* plane) around seals and rim cavity of secondary-air system.

primarily in the circumferential direction and only show this recirculating pattern of Fig. 6 when constrained to the *X*, *R* plane. The flow in the secondary-air system is difficult to visualize because one wall is stationary and the opposite wall (blade disk and TOBI pump) is rotating at the blade wheel speed. At the exit of the rim cavity where the flow merges with the main flowpath, it is useful to visualize the flow in both the stationary and rotating reference frames.

A close-up of the Mach number contours along with the streamlines around the a) labyrinth seals, b) inner TOBI seal, and c) rim cavity are shown in Fig. 7. Figure 7 shows the complexity of the

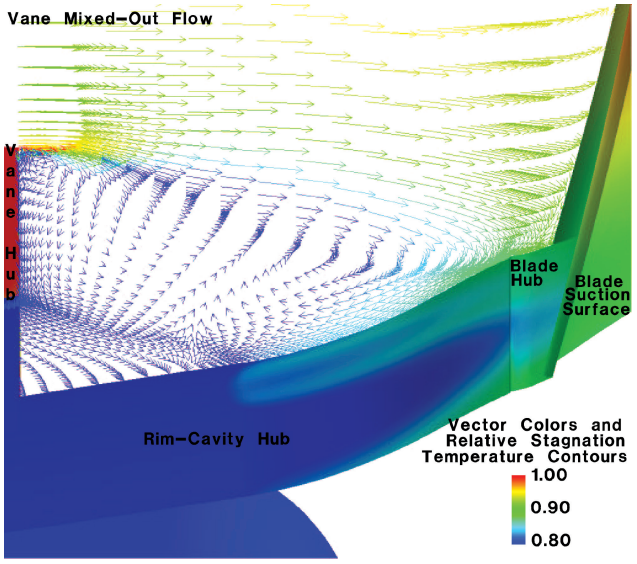

Fig. 8 Blade relative velocity vectors at rim-cavity exit along plane aligned with blade leading edge and relative stagnation temperature contours (vectors colored by relative stagnation temperature level).

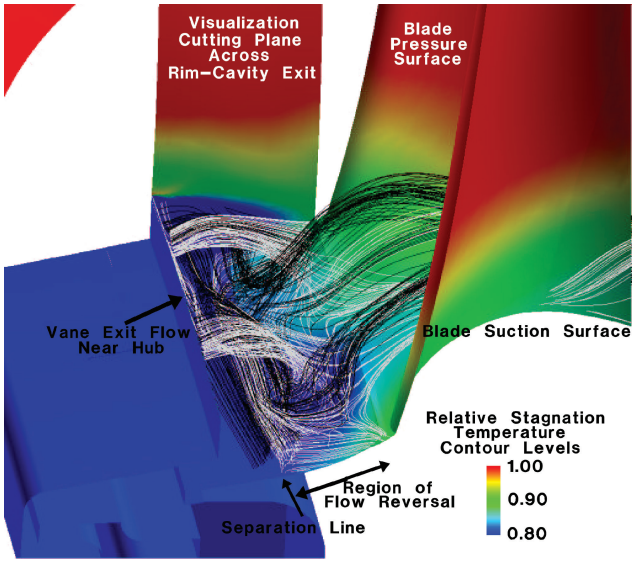

Fig. 9 Streamlines at rim-cavity exit and blade-relative stagnation temperature contours.

flow with large gradients through the seals and multiple regions of swirling, recirculating flow. In addition to the issues related to solution convergence mentioned earlier, these large gradients in localized regions of the flow can lead to numerical instabilities during convergence that also restrict the convergence rate of the procedure.

Figure 8 shows a close-up of the blade-relative velocity vectors and relative stagnation temperature contours at the junction between the rim-cavity exit and the main flowpath upstream of the blade hub. Figures 8 and 9, which shows the streamlines, give some indication of the complexity of the flow at this junction. The flow exiting the high-pressure vane flows over the rim-cavity exit where it stagnates on the blade hub endwall near the leading edge. At this location, the flow splits, with some of the flow reversing into the upper rim cavity where it meets with the rim-cavity exit flow, leading to a separation and a flow recirculation. This flow recirculation region is largest near the blade and smaller near midpitch. The complex streamline pattern at this junction is shown in Fig. 9. Figure 9 shows that the flow emerging from the rim cavity is not uniform across the pitch of the blade, but is affected by the blade endwall secondary flow and pressure field. Figures 8 and 9 show that a contributing factor

Table 1 Secondary-air system inlet/exit flow and absolute total pressure and temperature ratios of computational and network analyses holding flow splits

Parameter	Lower cavity centerline entrance	Lower cavity HPC bypass entrance	TOBI pump combustor bypass entrance	TOBI pump lower centerline exit	TOBI pump upper blade exit	Rim cavity exit
Flow ratio $\dot{m}/\dot{m}_{\text{main}}$	0.001	0.018	0.061	0.004	0.064	0.012
Computational $P_T/P_{T\text{main}}$	0.896	0.900	0.772	0.680	0.848	0.715
Network $P_T/P_{T\text{main}}$	0.550	0.556	1.047	0.347	0.601	0.483
Computational $T_T/T_{T\text{main}_{\text{max}}}$	0.304	0.477	0.431	0.565	0.531	0.895
Network $T_T/T_{T\text{main}_{\text{max}}}$	0.304	0.477	0.431	0.438	0.440	0.508

Table 2 Secondary-air system flow and absolute total pressure and temperature ratios of computational and network analyses predicting flow splits

Parameter	Lower cavity centerline entrance	Lower cavity HPC bypass entrance	TOBI pump combustor bypass entrance	TOBI pump lower centerline exit	TOBI pump upper blade exit	Rim cavity exit
Computational $\dot{m}/\dot{m}_{\text{main}}$	0.001	0.018	0.061	0.017	0.047	0.016
Network $\dot{m}/\dot{m}_{\text{main}}$	0.001	0.018	0.061	0.004	0.064	0.012
Computational $P_T/P_{T\text{main}}$	0.810	0.815	0.701	0.465	0.753	0.718
Network $P_T/P_{T\text{main}}$	0.550	0.556	1.047	0.347	0.601	0.483
Computational $T_T/T_{T\text{main}_{\text{max}}}$	0.304	0.477	0.431	0.520	0.532	0.885
Network $T_T/T_{T\text{main}_{\text{max}}}$	0.304	0.477	0.431	0.438	0.440	0.508

to reversal of main flowpath hot gases into the upper rim cavity may be the interaction between the rim-cavity exit flow and the secondary flow of the blade. Unsteady-flow simulations, as well as further steady-flow predictions, in which the mixing plane is placed at the blade leading edge to allow direct interaction between the vane exit and secondary-air system flow, are required to determine conclusively the primary contributors to hot-gas ingestion into the rim cavity.

Secondary-Air System Inlets/Exits

Table 1 gives a comparison of the absolute total temperature, and total pressure between the computational analysis, and the one-dimensional network analysis at the various inlets and exits of the secondary-air system. Table 1 shows that the total pressure at the inlet to the TOBI nozzle predicted by the coupled simulation was lower, but that the total pressure at the lower cavity entrances was higher than that determined by the network analysis. The lower total pressure at the TOBI pump entrance may be due to the differences in how the vanes at the exit of the TOBI pump are modeled between the two analyses.

Table 1 also shows that the predicted total pressure and total temperature leaving all of the secondary-air system exits in the coupled simulation are greater than that predicted by the network analysis. The higher total pressure exiting the secondary-air system could be the result of either 1) an underprediction of the losses in the coupled simulation relative to those predicted by the network analysis, 2) the overprediction of the total pressure necessary to hold the flow rates at the entrances to the lower cavity, and/or 3) an over-prediction of the swirl. An under prediction of secondary-air system losses could arise from a number of modeling issues including 1) how the actual holes in the TOBI pump are modeled as a slot with the same area, 2) the differences in how the TOBI nozzle flow and losses are modeled, and 3) the relatively low turbulence levels set at the entrance to the secondary-air system. The first two of these issues are related to the strategy in the current investigation to model the secondary-air system as an axisymmetric geometry to reduce computational resources. The results from the current investigation indicate that if the axisymmetric strategy is used, a loss model for the three-dimensional secondary-air system geometry effects would likely improve the computational results. Further numerical simulations, along with detailed experiments, are necessary to determine the sources of the differences between the computational and network analysis models.

In the interest of determining the ability of the current procedure to predict the secondary-air system flow splits, a second coupled simulation was run in which the static pressure was set at the exits of the secondary-air system based on the preliminary design network analysis. A listing of the resulting flow rates, total pressure, and total temperature at all of the secondary-air system inlets and exits is given in Table 2. Table 2 shows that the trends in the total pressure and total temperature at the inlets and exits are similar to the preceding simulation in which the flow splits were fixed. In addition, Table 2 shows that the predicted flow rate for the TOBI pump lower centerline exit is much greater, the flow rate for the TOBI pump upper blade exit is lower, and the predicted flow rate exiting the rim cavity is greater than that predicted by the network analysis. These results seem to indicate that the prediction of the flow splits may also depend on the accurate prediction of the stagnation pressure losses, including those due to three-dimensional geometry effects, in the secondary-air system.

Blade-Row Performance

An investigation of the sensitivity of the predicted temperature and aerodynamic performance to how the secondary-air system leakage flow was modeled was also performed. A comparison of the relative aerodynamic total pressure loss and entropy change across each blade row between the coupled simulation with fixed secondary-air system flow splits and two different isolated main flowpath simulations in which the leakage flow was modeled with a transpiration boundary condition is given in Table 3. Here, the total pressure loss and entropy change are simply found from the difference in the mass-averaged stagnation conditions between the main flowpath inlet and exit of each blade row. The TFLO solution procedure was used for all of these simulations. In the isolated main flowpath simulations, the mass flow rate and stagnation temperature of the transpiration leakage flow were prescribed by the use of Eq. (1) at the levels determined from the coupled simulation, as well as at those from the one-dimensional network analysis. Because the flow splits were held to those of the network analysis in the coupled simulation, the flow rate leaking into the main flowpath was the same for all three simulations. Likewise, all simulations converged to essentially the same main flowpath flow rate. The same main flowpath computational grid that was used in the coupled simulation was also used for the cases with transpiration leakage.

Table 3 shows that the losses predicted in all three blade rows are similar between the coupled simulation and the main flowpath simulation with transpiration if the leakage flow rate and total temperature are kept the same. This result indicates that the use of transpiration leakage models in isolated main flowpath simulations is reasonable for the prediction of aerodynamic performance if the details of the

Table 3 Relative total pressure and entropy change for each blade row with and without secondary-air leakage flow

Parameter	HPT vane	HPT blade	LPT vane
Relative total pressure loss $(P_{T_{\text{inlet}}} - P_{T_{\text{exit}}})/P_{T_{\text{inlet}}}$, coupled simulation	0.049	0.102	0.044
Relative total pressure loss $(P_{T_{\text{inlet}}} - P_{T_{\text{exit}}})/P_{T_{\text{inlet}}}$, transpiration at coupled conditions	0.041	0.103	0.044
Relative total pressure loss $(P_{T_{\text{inlet}}} - P_{T_{\text{exit}}})/P_{T_{\text{inlet}}}$, transpiration at network conditions	0.034	0.185	0.073
Entropy change $(S_{\text{exit}} - S_{\text{inlet}})/C_p$, coupled simulation	0.0192	0.0275	0.0111
Entropy change $(S_{\text{exit}} - S_{\text{inlet}})/C_p$, transpiration at coupled conditions	0.0130	0.0271	0.0111
Entropy change $(S_{\text{exit}} - S_{\text{inlet}})/C_p$, transpiration at network conditions	0.0141	0.0521	0.0197

interaction between the secondary-air system and main flowpaths are not considered important. Table 3 also shows that the losses in all three blade rows are substantially different if the leakage flow is modeled with the lower total temperature levels resulting from the network analysis. The losses in the HPT vane of the coupled simulation are greater than those of this isolated main flowpath simulation. In addition, the relative losses in the HPT blade and downstream LPT vane are lower for the coupled simulation compared to that of this isolated main flowpath simulation. These differences can be attributed to the higher total pressure, total temperature, and velocity exiting the rim cavity in the coupled simulation. In this case, the coupled rim-cavity exit flow increases the momentum of the hub flow downstream of the blade leading edge, resulting in a reduction in losses in the downstream blade rows. The higher total temperature of the secondary-air system flow in the coupled simulation also leads to a higher HPT vane exit Mach number and the emergence of a trailing-edge shock system. The interaction between the trailing-edge shock and the vane suction surface causes an increase in the boundary layer and wake thickness with a subsequent increase in the HPT vane total pressure loss. These results illustrate how the main flowpath blade-row aerodynamic performance can be significantly altered by the total temperature (and total pressure) levels of secondary-air system leakage flow.

The absolute temperature distribution on the hub of the main flowpath of the coupled simulation is shown in Fig. 10a. For comparison, the temperature contours along the hub resulting from the isolated main flowpath with the transpiration flow rate and total temperature set to that of the coupled simulation, via Eq. (1), are also shown in Fig. 10b. The hub endwall temperature distributions of all three blade rows are similar, except in the region between the vane exit and the midaxial chord position of the blade, where the coupled simulation predicts a lower temperature and a greater pitchwise variation of temperature than the isolated main flowpath simulation. The interaction between the leakage flow and the main flowpath is stronger in the coupled simulation, causing the higher-temperature main flowpath gas to be pushed slightly more away from the hub endwall. These results indicate that if the details of the endwall temperature distribution and flow interaction are important for durability predictions, then a direct coupling between the main flowpath and at least the rim-cavity flow should be considered. Otherwise, a transpiration model of the leakage flow can produce qualitatively similar results. The temperature contours of the isolated main flowpath simulation change dramatically, however, when the total temperature is held at that predicted by the preliminary design network analysis. For this case, as shown in Fig. 10c, the hub endwall temperature distributions changed in all three blade rows due to the lower temperature and momentum introduced into the main flowpath from the leakage flow. The high-temperature flow introduced at the inlet of the main flowpath now migrates to the vane endwall earlier in the vane passage compared to the simulations at the coupled leakage flow conditions. However, the lower-temperature air introduced in the leakage region of the isolated main flowpath simulation with network conditions compensates for the higher vane exit endwall temperature, resulting in slightly lower endwall temperatures for the blade and LPT vane. Similar to the aerodynamic performance results, these simulations show that the endwall temperature distributions are sensitive to the hub leakage flow total temperature (and total pressure).

Several physical and numerical issues have been illustrated in this baseline investigation. Further investigations are necessary,

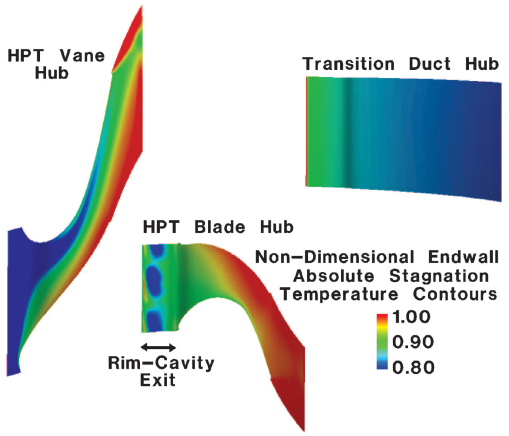

a) Coupled main/secondary simulation

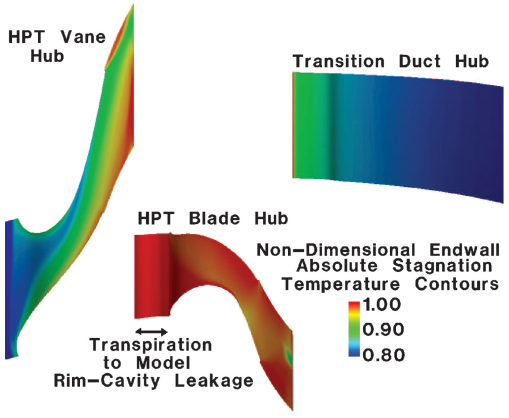

b) Isolated main flowpath simulation with secondary air modeled as transpiration leakage at coupled conditions

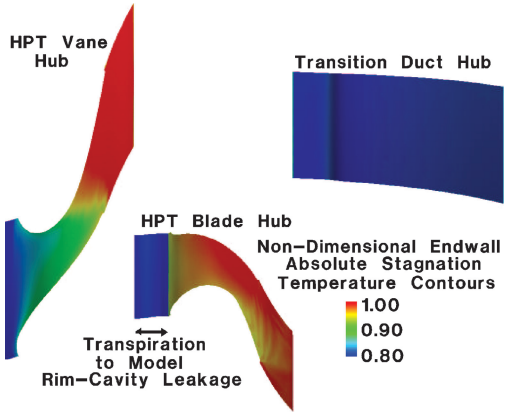

c) Isolated main flowpath simulation with secondary air modeled as transpiration leakage at network conditions

Fig. 10 Main flowpath hub absolute stagnation temperature contours.

however, to determine the effects of interblade mixing plane placement, secondary-air system inlet/exit boundary conditions, and losses due to three-dimensional secondary-air system geometry in coupled steady-flow simulations. In addition, further simulations are necessary to determine the differences between coupled steady-flow and unsteady-flow simulations. Because there can be significant unsteady pitchwise variations in the pressure, temperature, and velocity fields in the vicinity of the rim-cavity exit, unsteady-flow predictions and the resulting time average of the flow could also provide further insight into the complex flow physics in this region.

Conclusions

A steady, viscous flow simulation of the coupled main flowpath and secondary-air system for a modern jet engine HPT is presented and compared with results from a more traditional main flowpath simulation in which the secondary-air leakage flow is modeled with transpiration. The secondary-air system in the coupled simulation has been modeled as an axisymmetric geometry with three-dimensional flow in an attempt to simplify the computational model. Details of the initial and boundary conditions in the coupled simulation are described, along with a discussion of the solution convergence. Predicted temperature, Mach number, and streamlines are presented to illustrate the flow physics in the various regions of the flow. Predictions of the main flowpath aerodynamic losses and endwall temperature distributions of the coupled simulation are compare with isolated main flowpath simulations to illustrate the effect of leakage modeling.

Several issues have been highlighted in the current investigation:

1) Convergence of the numerical scheme is limited by regions of low-speed flow, high gradients in the flow during convergence, regions of choked flow around the seals, and the large gradients in the vicinity of the seals. Convergence acceleration schemes should be investigated to reduce solution times.

2) If an axisymmetric geometry is used in place of the actual geometry for the secondary-air system, then the losses and swirl production associated with the three-dimensional aspects must be modeled or predicted accurately. The accuracy of the flow split prediction, as well as the total temperature and pressure exiting the secondary-air system, is dependent on accurate prediction of the local secondary-air system total temperature and pressure fields.

3) Placement of the interblade-row mixing plane is dependent on the focus of the investigation. More simulations are required to determine the effects of placing the mixing plane at the blade leading edge as opposed to the vane hub trailing edge, as was performed in the current investigation. Steady-flow simulations should also be compared with time-averaged, unsteady-flow simulation results to highlight the errors associated with the steady-flow approach.

4) The results from the current investigation show that the blade-row aerodynamic losses predicted with a transpiration model for the hub leakage flow are similar to those resulting from the coupled simulation. In addition, the main flowpath hub endwall temperature distributions are also qualitatively similar between the two simulations, except in the vicinity and just downstream of the rim-cavity exit. However, if local details of the interaction of the leakage and main flowpaths are considered important, then a direct coupling of the two flowpaths should be performed.

5) Much more research in terms of both numerical investigations and detailed experiments are required to determine the specific strengths and weaknesses of coupled computational simulations such as the one attempted here. Not only validation with experimental data, but also further steady- and unsteady-flow numerical experiments are required to uncover modeling weaknesses and improve prediction accuracy for these system simulations.

Acknowledgments

The authors would like to thank the U.S. Department of Energy for its generous support under the Accelerated Strategic Computing Initiative program. The authors would especially like to recognize the support of the staff at the Lawrence Livermore National Laboratory. We would also like to thank the managers at Pratt and Whitney for their support. Finally, the authors would like to thank Edward Clutter for generating the secondary-air system computational grid for this investigation.

References

[1]Yao, J., Jameson, A., Alonso, J. J., and Liu, F., "Development and Validation of a Massively Parallel Flow Solver for Turbomachinery Flows," *Journal of Propulsion and Power*, Vol. 17, No. 3, 2001, pp. 659–668.

[2]Jameson, A., "Time Dependent Calculations Using Multigrid, with Applications to Unsteady Flows Past Airfoils and Wings," AIAA Paper 91-1596, June 1991.

[3]Wilcox, D. C., *Turbulence Modeling for CFD*, DCW Industries, Inc., La Cañada, CA, 1998.

[4]Yao, J., Davis, R. L., Alonso, J. J., and Jameson, A., "Massively Parallel Simulation of the Unsteady Flow in an Axial Turbine Stage," *Journal of Propulsion and Power*, Vol. 18, No. 2, 2002, pp. 465–471.

[5]Davis, R. L., Yao, J., Clark, J. P., Stetson, G., Alonso, J. J., Jameson, A., Haldeman, G. W., and Dunn, M. G., "Unsteady Interaction Between a Transonic Turbine Stage and Downstream Components," American Society of Mechanical Engineers, ASME Paper GT2002-39364, June 2002.

[6]Shankaran, S., Alonso, J. J., Liou, M., Liu, N., and Davis, R. L., "A Multi-Code-Coupling Interface for Combustor Turbomachinery Simulations," AIAA Paper 01-0974, Jan. 2001.